ChemElectroChem

Research Article
doi.org/10.1002/celc.202300103

Chemistry Europe
European Chemical Societies Publishing

www.chemelectrochem.org

Defect Engineering in Bimetallic NiFe-BTC for Boosting Electrocatalytic Oxygen Evolution Reaction through Coordinated Ionic Liquids

Ru Li[+],[a] Haodong Qi[+],[a] Fenghongkang Pan,[a, c] Wei Xie,[a] Lihui Zhou,[a] Honglai Liu,[a, b] and Jun Hu*[a]

Coordinatively unsaturated metal (CUM) sites in metal organic frameworks (MOFs) have demonstrated distinct catalytic activities, yet remain great challenges in their designing and engineering. Herein, a novel "Coordination Geometric Hindrance" approach based on ionic liquids (ILs) is proposed for defects construction in bimetallic MOF, of which the steric effect of competitively coordinated anions of imidazole ILs ([EMIM]X) enables the interference with the ordered growth of bimetallic NiFe-MOFs. Specifically, the PF_6^- anion displays the strongest binding energy with metals Ni and Fe, accordingly, facilitates the formation of CUM sites in NiFe-BTC/IL-PF_6. Taking both advantages of CUM defects and good intrinsic conductivity of IL, NiFe-BTC/IL-PF_6 achieves a superior electrocatalytic performance in the oxygen evolution reaction (OER), with the overpotential as low as 210 mV at 10 mA cm^{-2}, and the Tafel slope of 103 mV dec^{-1}, thus, giving an 18-fold larger TOF of the commercial OER catalyst of RuO_2.

Introduction

Striving for clean and sustainable hydrogen resource is one of the burning issues of the world to meet challenges of the Carbon Neutrality.[1] Catalytic water splitting by renewable energies has been considered as the most effective solution to this crisis.[2] However, the conversion efficiency and stability are far from expectations due to the slow kinetics of the multi-steps of proton-coupled electron transfer in the anodic oxygen evolution reaction (OER).[3] Great efforts have been devoted to find efficient electrocatalysts with more active sites, higher conductivity, and stability.[4] Among various electrocatalysts, metal-organic framework materials (MOFs) constructed by metal ions and organic ligands have been distinct catalytic applications due to their unique features such as large surface area, tunable porosity, a wide variety of metal node species.[5] However, their perfectly coordination, along with the inherently low electrical conductivity limit their electrocatalytic activities, consequently, greatly hinder further applications in OER.

Currently, rational designing strategies, such as synthesizing two-dimensional conductive MOFs[6] and building MOF nanoarrays,[7] as well as using MOFs as templates to obtain metal/carbon catalysts by pyrolysis[8] have been developed to enhance the conductivity and electrocatalytic performance.[9] However, difficulties in the precise control-synthesis for low-dimensional MOFs, and easy collapse of porous frameworks and agglomerations of metal sites during the pyrolysis make these strategies full of challenges.[10] In this regard, we draw on a contrary strategy of the defect engineering since the coordinatively unsaturated defects in MOFs have demonstrated distinct catalytic activities.[11] Wang et al created more coordinatively unsaturated metal (CUM) sites in ZIF-67 through the plasma etching, which significantly improved the OER performance. Moreover, they found the OER activity was reversely decreased by supplementing the missing ligands, demonstrating the contribution of defects.[12] Very recently, Tang et al. found that the bimetallic ratio in nodes would alter the geometric and electronic structure of MOF, accordingly, the in situ formed oxygen vacancies and high oxidation states of metals were responsible for their high OER activity.[13] Liu et al. reported an edge-enriched NiFe-layer double hydroxide nanosheet array. With abundant CUM sites, it offered high electrocatalytic activity in OER.[14] Therefore, deeply understanding how to develop more CUM sites, and in turn to enhance the catalytic activity and conductivity for the improved OER performance are highly desirable.

In this work, we carry out a novel "Coordination Geometric Hindrance" approach based on ionic liquids (ILs) for engineering

[a] R. Li,[+] H. Qi,[+] F. Pan, W. Xie, L. Zhou, Prof. H. Liu, Prof. J. Hu
Key Laboratory for Advanced Materials and
Joint International Research Laboratory for Precision Chemistry and Molecular Engineering
Feringa Nobel Prize Scientist Joint Research Center
School of Chemistry and Molecular Engineering
East China University of Science and Technology
Shanghai 200237 (P.R.China)
E-mail: junhu@ecust.edu.cn

[b] Prof. H. Liu
State Key Laboratory of Chemical Engineering and Department of Chemistry
East China University of Science and Technology
Shanghai 200237, (P.R.China)

[c] F. Pan
Societe Generale de Surveillance (Shanghai)
889 YiShan Road, Shanghai 200030, (P.R.China)

[+] These authors contributed equally to this work.

Supporting information for this article is available on the WWW under https://doi.org/10.1002/celc.202300103

defects in bimetallic MOFs. We anticipate that besides the intrinsic bimetallic enhancements for OER activity,[15] by using an IL-based co-solvothermal method, the anions of ILs can competitively coordinate with the metal nodes of MOF and interfere with the ordered growth of perfect crystals due to the geometric hindrance. In this way, more coordinatively unsaturated metal sites can be exposed. Meanwhile, the conductive ILs loading in channels enable to break through the conductivity limitation of MOFs. As expected, among various MOFs obtained by the imidazole ILs ([EMIM]X, X=NTf_2, PF_6, Cl, BF_4, or CF_3SO_3) co-solvothermal synthesis, NiFe-BTC/IL-PF_6 exhibits a superior OER performance, giving a low overpotential of 210 mV at 10 mA cm^{-2} and the significantly enhances TOF value is almost 18-fold larger than that of the commercial OER catalyst of RuO_2. Therefore, taking two advantages of defects' activity and ILs' conductivity together, we provide a promising defect engineering strategy to achieve highly efficient electrocatalytic OER performance.

Results and Discussion

Structural characteristics of NiFe-BTC/ILs

To achieve the proposed "Coordination Geometric Hindrance" induced defect engineering, suitable interference anions of imidazole ILs [EMIM]X (X=NTf_2^-, PF_6^-, Cl^-, BF_4^-, or $CF_3SO_3^-$) are selected by a DFT calculation. The calculated binding energies (BEs) of metal cation of Ni or Fe with the anions of ILs and the carboxyl group reveal the coordination capability is in the sequence of $PF_6^- > BF_4^- > NTf_2^- > Cl^- > CF_3SO_3^- > COO^-$, respectively (Figures 1b and S1). As the PF_6^- anion has almost twice stronger affinity toward Ni or Fe than COO^-, it can competitively replace the COO^- coordination during the solvothermal process. More importantly, unlike the commonly coordinated with small H_2O molecules, the larger geometric anion of PF_6^- together with the even larger joined counter cation of joined conter cations of $[EMIM]^+$ will hinder the nearby other coordination of COO^-, resulting in more coordinatively unsaturated oxygen sites.

The XRD patterns reveal the crystal structure changes under various ILs co-solvothermal synthesis (Figure S2a). In comparison with the simulated XRD pattern of Ni-BTC (CCDC no.636900), the characteristic peak of the (110) crystal plane at about 10.1° can be observed in NiFe-BTC and all NiFe-BTC/ILs, confirming their successful synthesis under various ILs co-solvothermal method. However, their slightly decreased intensity of the characteristic peaks reveals the structure change of their decreased crystallinity. In addition, the FTIR spetra of NiFe-BTC/ILs show the same characteristic peaks of trimesic acid ligand like C–O and C=O at 1260 cm^{-1} and 1700 cm^{-1}, and the benzene ring at 1510 cm^{-1} and 1540 cm^{-1}. Evidently, the appearance of characteristic peaks of different anions of imidazole ILs, such as the stretching vibration peaks of P–F at 864 cm^{-1}, C–F and S=O at 1414 cm^{-1}, 1175 cm^{-1} and B–F at 1165 cm^{-1} demonstrate the successful loading of [EMIM]X in NiFe-BTC/IL–Xs, respectively (Figure S3). The obtained NiFe-BTC/IL-PF_6 shows a similar ball-like morphology as NiFe-BTC, which is formed by aggregated MOF crystals, but more amorphous powders (Figure 1c, d). EDS-mapping images reveal evenly distributed elements of Fe, Ni, O and C. Significantly, the same highly distributed element F provide clear evidence that the PF_6^- anions are successfully coordinated in NiFe-BTC/IL-PF_6 (Figure 1e–h). As a result, the lower crystallinity of NiFe-BTC/ILs

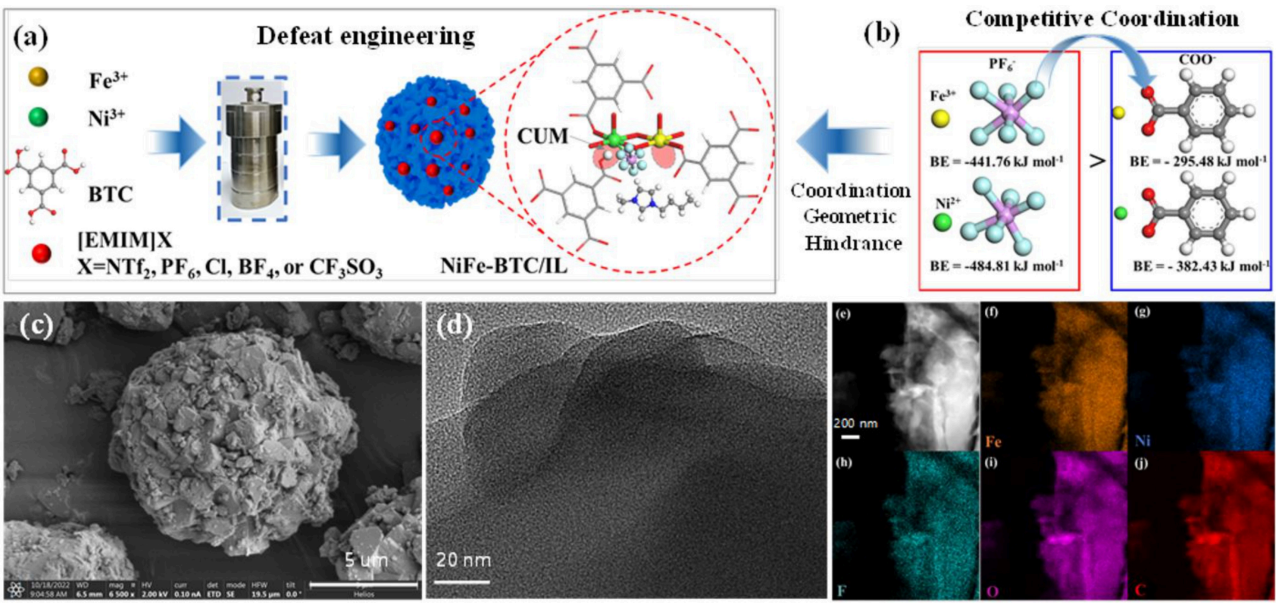

Figure 1. (a) Schematic illustration of the synthesis process and the IL-based "Coordination Geometric Hindrance" approach for engineering defects in NiFe-BTC/ILs. (b) Binding energies of metal of Ni or Fe with the PF_6^- and COO^-. (c) SEM (d) HR-TEM and (e-j) elemental mapping images of NiFe-BTC/IL-PF_6.(a) Schematic illustration of the synthesis process and the IL-based "Coordination Geometric Hindrance" approach for engineering defects in NiFe-BTC/ILs. (b) Binding energies of metal of Ni or Fe with the PF_6^- and COO^-. (c) SEM (d) HR-TEM and (e-j) elemental mapping images of NiFe-BTC/IL-PF_6.

comes naturally with the significantly decreased intensity of (110) peak, confirming the validity of our proposed defect engineering strategy of the "Coordination Geometric Hindrance".

Determined by N_2 adsorption/desorption isotherms at 77 K, the Brunauer-Emmett-Teller (BET) surface area of NiFe- BTC/ILs dramatically decrease due to these distorting defects and some blockages of ILs in the channels of MOFs (Figure S4). Typically, the BET surface area and the pore volume of NiFe-BTC/IL-PF_6 are only 175 $m^2 g^{-1}$ and 0.25 $cm^3 g^{-1}$, much smaller than those of NiFe-BTC of 280 $m^2 g^{-1}$ and 0.87 $cm^3 g^{-1}$ (Figure 2a). Whereas the major pore size of NiFe-BTC/IL-PF_6 is slightly increased from 1.38 nm to 1.66 nm, further indicating the dispersed ILs may interference the ordered growth of NiFe-BTC. Intuitively, the defect structure is confirmed by the EPR spectrum (Figure 2b). In comparison with NiFe-BTC, NiFe-BTC/IL-PF_6 gives a much larger intensity of the symmetrical resonance peaks, revealing the presence of more unpaired electrons, i.e. coordinately unsaturated metal sites. These changes of uncoordinated states are further illustrated by the X-ray photoelectron spectroscopy (XPS). In both O 1s XPS spectra, the peaks at 531.5 eV, 530.6 eV, 532.8 eV, and 531.6 eV, corresponding to metal-oxygen, lattice oxygen, water mole-cule-adsorbed oxygen, and coordination-unsaturated oxygen (O_{un}) can be observed (Figure 2c). It is noteworthy that the content of O_{un} gives a rise from 13% in NiFe-BTC to 30% in NiFe-BTC/IL-PF_6, suggesting the competitive coordination of PF_6^- anions with metal will leave more O_{un} vacancy in NiFe-BTC/IL-PF_6. Meanwhile, from the Fe 2p and Ni 2p XPS spectra of NiFe-BTC/IL-PF_6 (Figure S5), both Fe–O and Ni–O peaks show a shift towards lower binding energy, again confirming the weaken coordination of COO^-. What's more, along with the feature that defects in metal oxides can usually cause the appearance of new peaks in Raman spectra,[16] two new peaks appear at 486 cm^{-1} and 589 cm^{-1} on the Raman spectra of NiFe-BTC/IL-PF_6 provide clear evidence of defects (Figure 2d). All these together demonstrate that the presence of ILs can effectively interfere with the COO–M coordination, which distort the ordered growth of organometallic framework structure, thus exposing more defects of CUM and O_{un} vacancy to enhance the catalytic activity.

Electrocatalytic OER performance

As a proof-of-concept, the electrocatalytic OER performance of NiFe-BTC/ILs are evaluated by the overpotential at 10 mA cm^{-2} in 1.0 M KOH solution (Figure 3a). Consistent with the DFT prediction, the linear sweep voltammetry (LSV) curve of NiFe-BTC/IL-PF_6 gives the best OER activity among all the NiFe-BTC/ILs modulated by different kinds of anions, demonstrating the validity of our defect engineering approach. To elaborate upon the importance of defects for the OER performance, we regulate the amount of [EMIM]PF_6 in the solvothermal process (Figure 3b). As a result, it shows a volcanic change that the OER performance improved with the adding amount of ILs, but too many amounts will lead to the decline of performance. The

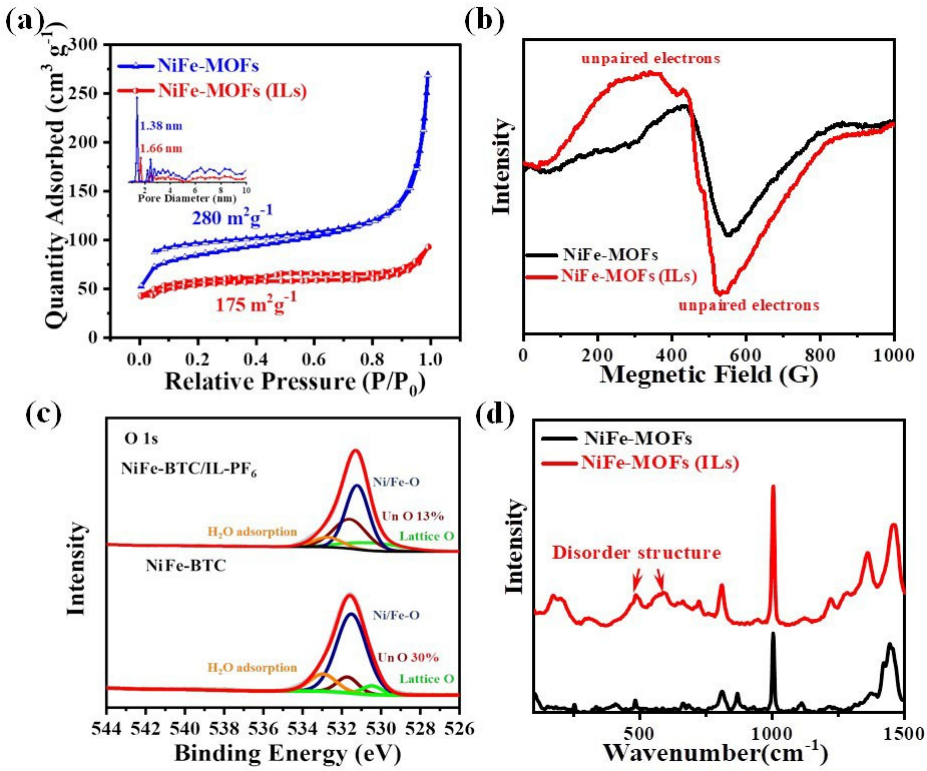

Figure 2. (a) N_2 adsorption/desorption isotherms and the insert of pore size distributions. (b) EPR (c) O 1S XPS spectra and (d) Raman spectra of NiFe-BTC/IL-PF_6 and NiFe-BTC.

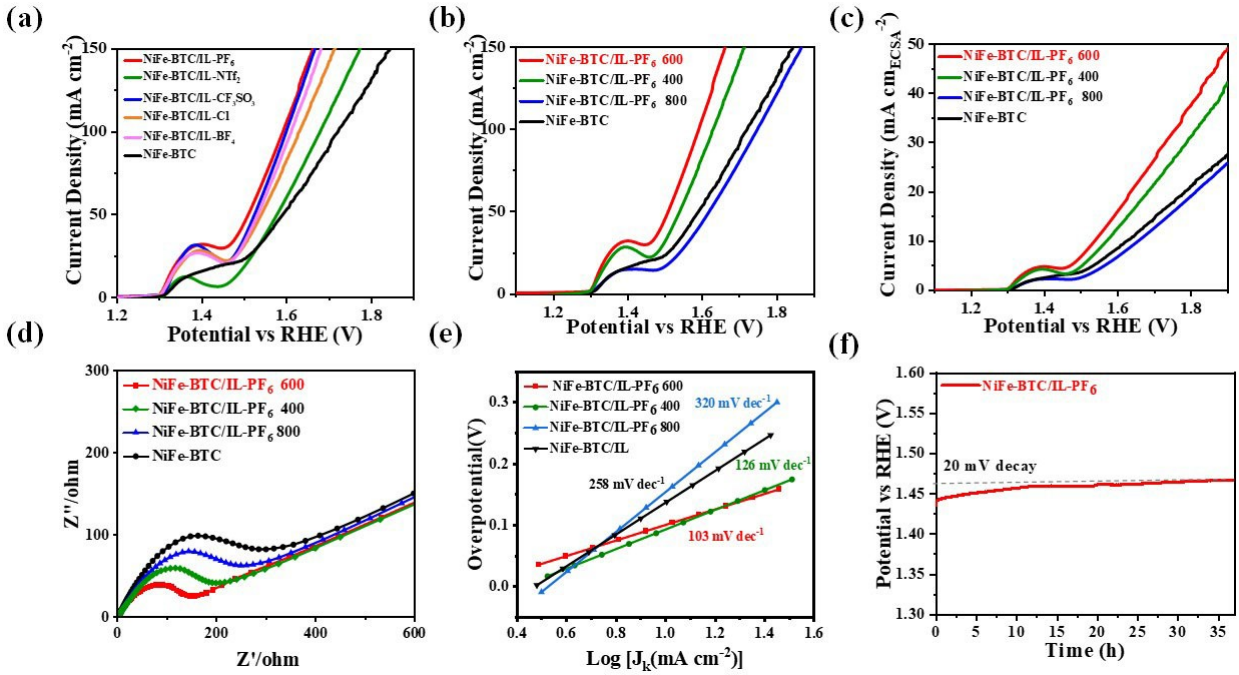

Figure 3. (a) LSV curves of NiFe-BTC/ILs with different kinds of anions, (b) LSV curves of NiFe-BTC/IL-PF_6 with different amounts of [BMIM]PF_6 addition. (c) Chronopotentiometry test (U-t) of NiFe-BTC/IL-PF_6 and NiFe-BTC. (d) EIS and (e) Tafel slopes spectra of the Ni-BTC, NiFe-BTC, and NiFe-BTC/ILs with different amounts of [BMIM]PF_6 addition. (f) Stability of NiFe-BTC/ILs in 0.1 M KOH.

corresponding ECSA-normalized LSV curves (Figure 3c) display that the required overpotential of NiFe-BTC/IL-PF_6-600 is the smallest to achieve the same current density, due to its higher inherent activity. Specifically, NiFe-BTC/IL-PF_6-600, with adding 600 mg [EMIM]PF_6, achieves the best OER performance that the overpotential requires only 210 mV to give the current densities of 10 mA cm^{-2}, which exceeds that of commercial OER catalysts of RuO_2 (330 mV) and IrO_2 (310 mV), respectively. More significantly, 280 mV overpotential is required to give a much higher current densities of 50 mA cm^{-2}. Such changing pattern of the OER performance provides clear evidence that suitable defects in NiFe-BTC/ILs is crucial to enhance the OER performance, while too many defects will cause the frameworks collapse, and inevitably lose the catalytic activity. As the main electrocatalytic sites of Ni^{2+}-Ni^{3+} oxidation peaks in the LSV curve overlapped the accurate determination of the overpotential at a current density of 10 mA cm^{-2} (Figure S6), we carry out the chronopotentiometry test (U-t) at a fixed current density of 10 mA cm^{-2} (Figure S7). Comparing with the U-t curve of NiFe-BTC, it provides a confident proof of much lower overpotential of 210 mV on NiFe-BTC/IL-PF_6-600, superior to most reported NiFe bimetallic electrocatalysts so far as we know (Table S1). Consistent with the OER performance on the working electrode of the nickel foam substrate, when the glass carbon is taken as the substrate, the linear sweep voltammetry (LSV) curve of NiFe-BTC/IL-PF_6 produced in the solvothermal process with adding 600 mg [EMIM]PF_6 gives the best OER activity among all the NiFe-BTC/ILs modulated by different kinds of anions and dosages (Figure S8). More significantly, the overpotential of NiFe-BTC/IL-PF_6-600 of 215 mV at 10 mA cm^{-2} on the glass carbon is only slightly higher than that on the nickel foam, demonstrating the excellent pristine OER performance of NiFe-BTC/IL-PF_6-600. Further CV tests at different scan rates reveal the inherent structure for this excellent performance. Deduce from the slope of the current intensity double layer capacitance (Cdl) than that NiFe-BTC (Figure S9), suggesting the active electrochemical surface area (ECSA), i.e. the number of active sites are significantly increased due to the successful defect engineering.

We measure the intrinsic charge transfer properties by the electrochemical impedance spectroscopy (EIS) to further demonstrate the contribution of ILs conductivity. From the Nyquist plots, we can see the radius of semicircle in the low frequency region decrease with adding ILs, again, NiFe-BTC/IL-PF_6-600 shows the fastest charge transfer performance, confirming the good conductivity of ILs enables the decrease of the intrinsic charge transfer resistance (Figure 3d). Combing both excellent electrocatalytic activity caused by the defects and the low charge transfer resistance by the ILs, NiFe-BTC/IL-PF_6-600 achieves extremely rapid OER catalytic kinetics, of which the Tafel slope is calculated as low as 103 mV dec^{-1}, less a half of 258 mV dec^{-1} of NiFe-BTC, superior to all the other control samples (Figure 3e).

Comprehensively, the TOF value of NiFe-BTC/IL-PF_6 is calculated as high as 144.6 h^{-1}, more than 18-folds of that of commercial OER catalyst of RuO_2 (8.03 h^{-1}). More significantly, during a long-term of 37 h chronopotentiometry, the overpotential of NiFe-BTC/IL-PF_6 increases by only 20 mV at a constant current density of 10 mA cm^{-2} (Figure 3f). The content of IL in electrolytes after OER is detected by the Inductively

Coupled Plasma Optical Emission Spectrometer (ICP-OES), the mole ratio of P and [EMIM]PF_6 is 1:1, thus we detect the content of P to confirm the stability of loaded ILs. It turns out the content of P in NiFe-BTC/IL-PF_6 is 0.023 mg/mg. When 1 mg NiFe-BTC/IL-PF_6 is dispersed on the electrode, after the electrolysis, the content of P in electrolytes is 0.020 mg L^{-1}. As the electrolytes is 70 ml, then the total leaching amount of P is 0.0014 mg, which can be neglected in comparison with the loading amount of P in NiFe-BTC/IL-PF_6, proving a good stability of NiFe-BTC/IL-PF_6. Moreover, after the OER process, no significant changes can be observed in the XRD patterns of NiFe-BTC/ILs, demonstrating their excellent stability. (Figure S2b) Thus, through the defect engineering of "Coordination Geometric Hindrance", NiFe-BTC/IL-PF_6 achieves an excellent intrinsic catalytic activity for OER.

Conclusion

In summary, we develop a novel "Coordination Geometric Hindrance" defect engineering approach. By making use of the geometrical size of anions in ILs [EMIM]X, the easily coordinated anions replace the carboxyl coordination to interfere with the ordered growth of NiFe-MOFs. Specifically, PF_6^- displays the strongest BE with metals Ni and Fe, accordingly, facilitating the defect formation of CUM sites and oxygen vacancy in NiFe-BTC/IL-PF_6 through the IL-co-solvothermal. As a result, an excellent OER catalytic activity is achieved with the overpotential as low as 210 mV at 10 mA cm^{-2}. Meanwhile, taking the advantages of high conductivity of loaded ILs, the rapid dynamics of OER is reached with the Tafel slope as low as 103 mV dec^{-1}. Therefore, this work provides a facile method for constructing defect-rich MOFs, which has great potential for applications in enhancing the electrocatalytic OER performance of MOF materials and opens a new path for rational design of high-performance catalysts.

Experimental Section

Reagents. Trimesic acid(H_3BTC), $Ni(NO_3)_2 \cdot 6H_2O$, $Fe(NO_3)_3 \cdot 9H_2O$ and isopropanol were purchased from Sinopharm Chemical Reagent Co. N,N-dimethylformamide (DMF), ILs of [EMIM]NTf_2, [EMIM]PF_6, [EMIM]Cl, [EMIM]BF_4, [EMIM]CF_3SO_3 were purchased from Shanghai Titan Technology Co. Naphthol was purchased from Alfa Aesar (China) Chemical Co. All chemicals were used as purchased without any further treatments.

Synthesis of NiFe-BTC/ILs. The schematic synthesis of NiFe-BTC/ILs by an IL-based solvothermal method is illustrated in Figure 1a. Typically, 0.793 g of $Ni(NO_3)_2 \cdot 6H_2O$, 0.11 g $Fe(NO_3)_3 \cdot 9H_2O$ and 0.3 g H_3BTC were dissolved in 60 mL DMF. By adding 400–800 mg ILs of [EMIM]NTf_2, [EMIM]PF_6, [EMIM]Cl, [EMIM]BF_4, or [EMIM]CF_3SO_3, respectively, the whole solution transferred into 100 ml Teflon-lined stainless autoclave after the sonication for 30 mins. Then, it was maintained at 125 °C for 10 h in an oven for the crystallization. After cooling naturally to the room temperature, the suspension was centrifuged, washed with DMF for three times, and dried at 80 °C for 12 hours to obtain the NiFe-BTC/ILs.[17]

Meanwhile, without adding ILs, NiFe-BTC was also synthesized by the same method as a control sample.

Characterizations. Transmission electron microscope (TEM) images and EDS of samples were obtained by transmission electron microscope (JEOL JEM-2100) with an accelerating voltage of 200 kV. SEM images were obtained by scanning electron microscope (JEOL JEM-6360) with an accelerating voltage of 15 kV. The crystalline structures of the samples were obtained by powder X-ray diffraction (PXRD, D/Max-2550VB/PC diffractometer) with a Cu Kα source, a tube voltage of 40 kV and a tube current of 200 mA. The content and valence distribution of the elements were obtained by inductively coupled plasma-emission spectrometry (Agilent 725 ICP-OES) and X-ray photoelectron spectroscopy (ESCALAB 250Xi). The surface structure of the samples was obtained by Raman spectroscopy as well as electron paramagnetic resonance spectroscopy (EMX-8/2.7). The specific surface areas of the samples were obtained by nitrogen adsorption and desorption tests on a Micrometrics tristar 3020 volume adsorption analyzer. The samples were dried at 120 °C under nitrogen atmosphere for 5 h before testing. The Brunauer-Emmett-Teller (BET) equation and the Barrett-Joyner-Halenda (BJH) model were used to calculate parameters such as the comparative area and pore size distribution of the samples obtained. Thermo Scientific Nicolet iS10 instrument was used to record the Fourier Transform Infrared (FTIR) spectra of the samples.

Electrode preparation Firstly, a piece of nickel foam (NF, 2 cm × 1 cm) was sonicated in hydrochloric acid (1 M), acetone and anhydrous ethanol for 30 min, and then dried in a blast drying oven at 80 °C for 1 h. Next, 5 mg of catalyst powder was added to the sample vial, followed by 666 μL of deionized water, 333 μL of ethanol and 30 μL of naphthol dispersion (5% by mass), and then sonicated for 1 hour. Finally, 200 μL of the dispersion was added dropwise to a nickel foam (area of 1 cm^2) and placed under an infrared lamp for drying. As comparison, all other samples and commercially available ruthenium dioxide powder-loaded electrodes were prepared in the same way.

Computational details. The fragments of H_3BTC ligand of COO^-, the anions of [EMIM]X ILs, X=NTf_2^-, PF_6^-, Cl^-, BF_4^-, or $CF_3SO_3^-$, and Fe^{3+}, Ni^{2+} were optimized using the DMol3 module of Material Studio. The Perdew-Burke-Ernzerhof (PBE) generalization function of the generalized gradient approximation (GGA) and the double numerical orbital basis group (DNP)[18] were used in the DFT calculations. Considering that there is interaction between Fe^{3+}, Ni^{2+} and $COOH^-$, PF_6^-, BF_4^-, Cl^- fragments, D2 method of GRIME (DFT–D) was chosen to calculate the binding energy (BE) and each electrostatic potential density.

Supporting Information

Additional references cited within the Supporting Information.[19–35]

Acknowledgements

We acknowledge the financial support from the National Natural Science Foundation of China (Nos. 22250005, 22278126), Intergovernmental Science and Technology Innovation Cooperation Key Project (2021YFE0112800) and the Fundamental Research Funds for the Central Universities (2022ZFJH004)

Conflict of Interests

The authors declare no conflict of interest.

Data Availability Statement

The data that support the findings of this study are available from the corresponding author upon reasonable request.

Keywords: Defect engineering · metal organic frameworks · Ionic liquids Electrocatalytic activity · Oxygen evolution reaction

[1] a) S. Chu, A. Majumdar, *Nature* **2012**, *488*, 294–303; b) A. Sahasrabudhe, H. Dixit, R. Majee, S. Bhattacharyya, *Nat. Commun.* **2018**, *9*, 2014.
[2] a) J. Zhu, L. S. Hu, P. X. Zhao, L. Y. S. Lee, K.-Y. Wong, *Chem. Rev.* **2020**, *120*, 851–918; b) M. Kuang, G. F. Zheng, *Small* **2016**, *12*, 5656–5675.
[3] a) J. Suntivich, K. J. May, H. A. Gasteiger, J. B. Goodenough, Y. Shao-Horn, *Science* **2011**, *334*, 1383–1385; b) C. Tang, H.-F. Wang, Q. Zhang, *Acc. Chem. Res.* **2018**, *51*, 881–889.
[4] a) X. Y. Peng, L. B. Zeng, D. S. Wang, Z. B. Liu, Y. Li, Z. J. Li, B. Yang, L. C. Lei, L. M. Dai, Y. Hou, *Chem. Soc. Rev.* **2023**, *52*, 2193–2237; b) Q. Chen, S. K. Xian, X. L. Dong, Y. Y. Liu, H. Wang, D. H. Olson, L. J. Williams, Y. Han, X.-H. Bu, J. Li, *Angew. Chem. Int. Ed.* **2021**, *60*, 10593–10597; c) M.-H. Yu, B. Space, D. Franz, W. Zhou, C. H. He, L. B. Li, R. Krishna, Z. Chang, W. Li, T.-L. Hu, X.-H. Bu, *J. Am. Chem. Soc.* **2019**, *141*, 17703–17712.
[5] a) Z. Y. Di, C. P. Liu, J. D. Pang, C. Chen, F. Hu, D. Q. Yuan, M. Y. Wu, M. C. Hong, *Angew. Chem. Int. Ed.* **2021**, *60*, 10828–10832; b) L. J. Kong, M. Liu, H. Huang, Y. H. Xu, X.-H. Bu, *Adv. Energy Mater.* **2022**, *12*, 2100172; c) J. He, N. Li, Z.-G. Li, M. Zhong, Z. X. Fu, M. Liu, J. C. Yin, Z. Shen, W. Li, J. Zhang, Z. Chang, X.-H. Bu, *Adv. Funct. Mater.* **2021**, *31*, 2103597.
[6] M. K. Cai, Q. L. Liu, Z. Q. Xue, Y. L. Li, Y. N. Fan, A. P. Huang, M.-R. Li, M. Croft, T. A. Tyson, Z. F. Ke, G. Q. Li, *J. Mater. Chem. A* **2020**, *8*, 190–195.
[7] a) D. Zhou, J. F. Ni, L. Li, *Nano Energy* **2019**, *57*, 711–717; b) Y. C. Wu, W. Wei, R. H. Yu, L. X. Xia, X. F. Hong, J. X. Zhu, J. T. Li, L. Lv, W. Chen, Y. Zhao, L. Zhou, L. Q. Mai, *Adv. Funct. Mater.* **2022**, *32*, 2110910; c) J. X. Zhu, S. K. Li, Z. C. Zhuang, S. Gao, X. F. Hong, X. L. Pan, R. H. Yu, L. Zhou, L. V. Moskaleva, L. Q. Mai, *Energy Environ. Mater.* **2022**, *5*, 231–237.
[8] a) Y. T. Hu, C. Song, C. J. Li, J. Wang, *J. Mater. Chem. A* **2022**, *10*, 8172–8177; b) Y. J. Chen, S. F. Ji, C. Chen, Q. Peng, D. S. Wang, Y. D. Li, *Joule* **2018**, *2*, 1242–1264.
[9] a) C. Li, H. Zhang, M. Liu, F.-F. Lang, J. Pang, X.-H. Bu, *Ind. Chem. Mater.* **2023**, *1*, 9–38; b) J. X. Zhu, L. X. Xia, W. X. Yang, R. H. Yu, W. Zhang, W. Luo, Y. H. Dai, W. Wei, L. Zhou, Y. Zhao, L. Q. Mai, *Energy Environ. Mater.* **2022**, *5*, 655–661.
[10] H. L. Jiang, Q. He, Y. K. Zhang, L. Song, *Acc. Chem. Res.* **2018**, *51*, 2968–2977.
[11] a) R. R. Zhang, L. Pan, B. B. Guo, Z. F. Huang, Z. X. Chen, L. Wang, X. Zhang, Z. Y. Guo, W. Xu, K. P. Loh, J.-J. Zou, *J. Am. Chem. Soc.* **2023**, *145*, 2271–2281; b) Y. F. Lin, H. Wan, D. Wu, G. Chen, N. Zhang, X. H. Liu, J. H. Li, Y. J. Cao, G. Z. Qiu, R. Z. Ma, *J. Am. Chem. Soc.* **2020**, *142*, 7317–7321; c) J. X. Zhu, L. X. Xia, R. H. Yu, R. H. Lu, J. T. Li, R. H. He, Y. C. Wu, W. Zhang, X. F. Hong, W. Chen, Y. Zhao, L. Zhou, L. Q. Mai, Z. Y. Wang, *J. Am. Chem. Soc.* **2022**, *144*, 15529–15538.
[12] L. Tao, C. Y. Lin, S. Dou, S. Feng, D. W. Chen, D. D. Liu, J. Huo, Z. H. Xia, S. Y. Wang, *Nano Energy* **2017**, *41*, 417–425.
[13] S. L. Zhao, C. H. Tan, C.-T. He, P. F. An, F. Xie, S. Jiang, Y. F. Zhu, K.-H. Wu, B. W. Zhang, H. J. Li, J. Zhang, Y. Chen, S. Q. Liu, J. C. Dong, Z. Y. Tang, *Nat. Energy* **2020**, *5*, 881–890.
[14] B. Q. Wang, X. Han, C. Guo, J. Jing, C. Yang, Y. Q. Li, A. J. Han, D. S. Wang, J. Liu, *Appl. Catal. B* **2021**, *298*, 120580.
[15] a) F. H. K. Pan, K. Huang, P. Liu, R. Li, C. Lian, H. L. Liu, J. Hu, *Small Structures* **2022**, *3*, 2200094; b) F. K. Pan, T. Jin, W. Yang, H. Li, Y. Cao, J. Hu, X. Zhou, H. L. Liu, X. Z. Duan, *Chem Catal.* **2021**, *1*, 734-745; c) P. F. Zhang, X. Y. Deng, W. Li, Z. Z. Ma, X. G. Wang, *Chem. Eng. J.* **2022**, *449*, 137886.
[16] K. H. Ye, K. S. Li, Y. R. Lu, Z. J. Guo, N. Ni, H. Liu, Y. C. Huang, H. B. Ji, P. S. Wang, *TrAC Trends Anal. Chem.* **2019**, *116*, 102–108.
[17] C. Wang, L. Chai, C. Luo, S. L. Liu, *Appl. Surf. Sci.* **2021**, *540*, 148336.
[18] a) J. A. White, D. M. Bird, *Phys. Rev. B* **1994**, *50*, 4954–4957; b) J. P. Perdew, J. A. Chevary, S. H. Vosko, K. A. Jackson, M. R. Pederson, D. J. Singh, C. Fiolhais, *Phys. Rev. B* **1992**, *46*, 6671–6687.
[19] X. T. Ling, F. Du, Y. T. Zhang, Y. Shen, T. Li, A. Alsaedi, T. Hayat, Y. Zhou, Z. G. Zou, *RSC Adv.* **2019**, *9*, 33558–33562.
[20] G. T. Hai, X. L. Jia, K. Y. Zhang, X. Liu, Z. Y. Wu, G. Wang, *Nano Energy* **2018**, *44*, 345–352.
[21] C. Q. Li, Y. W. Liu, G. Wang, L. H. Guan, Y. Q. Lin, *ACS Sustainable Chem. Eng.* **2019**, *7*, 7496–7501.
[22] J. T. Li, W. Z. Huang, M. M. Wang, S. B. Xi, J. S. Meng, K. N. Zhao, J. Jin, W. W. Xu, Z. Y. Wang, X. Liu, Q. Chen, L. H. Xu, X. B. Liao, Y. L. Jiang, K. A. Owusu, B. L. Jiang, C. X. Chen, D. N. Fan, L. Zhou, L. Q. Mai, *ACS Energy Lett.* **2019**, *4*, 285–292.
[23] Z. Wang, J. Xu, J. H. Yang, Y. H. Xue, L. M. Dai, *Chem. Eng. J.* **2022**, *427*, 131498.
[24] L. Gong, X. Y. E. Chng, Y. H. Du, S. B. Xi, B. S. Yeo, *ACS Catal.* **2018**, *8*, 807–814.
[25] F. Song, X. L. Hu, *Nat. Commun.* **2014**, *5*, 4477.
[26] C. Roy, B. Sebok, S. B. Scott, E. M. Fiordaliso, J. E. Sørensen, A. Bodin, D. B. Trimarco, C. D. Damsgaard, P. C. K. Vesborg, O. Hansen, I. E. L. Stephens, J. Kibsgaard, I. Chorkendorff, *Nat. Catal.* **2018**, *1*, 820–829.
[27] J. Ahn, Y. S. Park, S. Lee, J. Yang, J. Pyo, J. Lee, G. H. Kim, S. M. Choi, S. K. Seol, *Sci. Rep.* **2022**, *12*, 346.
[28] B. Wu, S. Gong, Y. Lin, T. Li, A. Chen, M. Zhao, Q. Zhang, L. Chen, *Adv. Mater.* **2022**, *34*, 2108619.
[29] C. Roy, B. Sebok, S. B. Scott, E. M. Fiordaliso, J. E. Sørensen, A. Bodin, D. B. Trimarco, C. D. Damsgaard, P. C. K. Vesborg, O. Hansen, I. E. L. Stephens, J. Kibsgaard, I. Chorkendorff, *Nano Energy* **2020**, *68*, 104293.
[30] C. J. Xuan, J. Wang, W. W. Xia, Z. K. Peng, Z. X. Wu, W. Lei, K. D. Xia, H. L. Xin, D. Wang, *ACS Appl. Mater. Interfaces* **2017**, *9*, 26134–26142.
[31] Y. R. Shen, L. Wang, P. P. Jiang, W. S. V. Lee, J. M. Xue, *ChemElectroChem* **2019**, *6*, 2741–2747.
[32] F. Song, M. M. Busch, B. Lassalle-Kaiser, C.-S. Hsu, E. Petkucheva, M. Bensimon, H. M. Chen, C. Corminboeuf, X. Hu, *ACS Cent. Sci.* **2019**, *5*, 558–568.
[33] X. Q. Mu, H. M. Yuan, H. Y. Jing, F. J. Xia, J. S. Wu, X. Y. Gu, C. Y. Chen, J. C. Bao, S. L. Liu, S. Mu, *Appl. Catal. B* **2021**, *296*, 120095.
[34] X. Long, J. K. Li, S. Xiao, K. Y. Yan, Z. L. Wang, H. N. Chen, S. H. Yang, *Angew. Chem. Int. Ed.* **2014**, *53*, 7584–7588.
[35] X. Y. Lu, C. Zhao, *Nat. Commun.* **2015**, *6*, 6616.

Manuscript received: March 28, 2023
Revised manuscript received: April 26, 2023
Version of record online: June 1, 2023